

Spectral synthesis of 3D unified model atmospheres with winds for O stars

L. Delbroek, J.O. Sundqvist, D. Debnath, N. Moens, F. Backs, C. Van der Sijpt, O Verhamme, and P. Schillemans

Institute of Astronomy, KU Leuven, Celestijnenlaan 200D, bus 2401, 3001 Leuven, Belgium

Received MONTH DAY, YEAR; accepted MONTH DAY, YEAR

ABSTRACT

Context. Spectroscopic studies of massive and luminous O-type stellar atmospheres and winds have primarily been done by using one-dimensional (1D), spherically symmetric and stationary models. However, both observations and modern theoretical models show that such O stars have highly structured and variable atmospheres and winds.

Aims. We present first spectral synthesis based on three-dimensional (3D) time-dependent unified radiation-hydrodynamic (RHD) model atmospheres with winds for O stars.

Methods. We first carried out time-dependent, 3D simulations of unified O star atmospheres with winds. We then used 3D radiative transfer to compute surface brightness maps for the optical continuum as well as integrated flux profiles for select diagnostic lines. To derive occupation numbers and source functions, an approximate non-local thermodynamic equilibrium (aNLTE) method was used, as well as scattering source functions.

Results. Our continuum intensity maps of a prototypical early O star ($\langle T_{\text{eff}} \rangle = 40.2$ kK, $\log_{10} (\langle L_{\star} \rangle / L_{\odot}) = 5.79$) in the Galaxy reveal a highly variable and time-dependent surface, characterised by local emergent radiation temperature variations exceeding 10 000 K. Our averaged synthetic line profiles of optical absorption lines have large widths, $\sigma \approx 50$ -60 km/s, without applying any macro- or microturbulence. From the RHD simulations we find correspondingly large velocity dispersions of $\sigma \approx 50$ -60 km/s in the photospheric layers. Additionally, the absorption line equivalent widths (EWs) are larger than for comparable 1D models. First results using scattering source functions further demonstrate that characteristic features like the softening of the blue edge of strong ultra-violet wind lines are qualitatively well-reproduced by our models.

Conclusions. Our 3D simulations clearly predict a highly structured and strongly variable O star surface, in stark contrast with the smooth surfaces assumed by the 1D models currently used for quantitative spectroscopy of such stars. First line profile results further suggest that several observed features are naturally reproduced by our models without the need to introduce ad-hoc spectral fitting parameters. We also discuss how using 3D rather than 1D simulations as a basis for future studies may affect the derivation of fundamental stellar parameters like surface gravities and chemical abundances.

Key words. Stars: massive - Stars: atmospheres - Stars: winds - Methods: numerical - hydrodynamics, radiative transfer

1. Introduction

Traditionally, the assumptions of a spherically symmetric, stationary one-dimensional (1D) atmosphere and wind have been made in spectroscopic studies of O stars (for example Hillier & Miller 1998; Kudritzki & Puls 2000; Puls et al. 2005; Sander et al. 2012). However, theoretical studies have long indicated that the coupled envelopes, atmospheres and line-driven winds (Castor et al. 1975) of O stars are highly structured and variable (due to convective and radiative envelope instabilities, as well as wind instabilities, Hearn 1972; Owocki & Rybicki 1984; Blaes & Socrates 2003; Cantiello et al. 2009; Jiang et al. 2015; Van der Sijpt et al. 2025; Key et al. 2025). Other strong indications can be found in various observed phenomena, for example optical absorption lines which indicate very large ‘micro’ and/or ‘macroturbulent’ velocities (the latter even going up to > 100 km/s, see for example Simón-Díaz et al. 2017a), optical emission lines that show line profile variability, and ‘wind clumping’ (Conti & Ebbets 1977; Eversberg et al. 1998; Puls et al. 2006; Sundqvist et al. 2010; Simón-Díaz et al. 2017b).

Recently, we performed time-dependent, two-dimensional (2D) unified simulations of O star atmospheres with winds using a flux-limiting radiation-hydrodynamical (RHD) finite vol-

ume modelling technique, accounting properly for the effects of line-driving (Debnath et al. 2024). In these simulations, opacities are computed using a hybrid approach (Poniatowski et al. 2021), which combines tabulated Rosseland mean opacities with calculations of the enhanced line opacities expected for supersonic flows. The latter are here based on the Sobolev (1960) approximation. In these simulations then, structure formation can already be found just below the iron-opacity peak (located at approximately 200 kK, Iglesias & Rogers 1996). By means of radiative acceleration exceeding gravity, local pockets of gas shoot up from these deep layers into the atmosphere above. Once in the upper atmosphere, these pockets then interact with the overlaying line-driven wind outflow, creating a highly structured, turbulent atmosphere. This interaction also gives rise to large turbulent velocities in the photospheric layers of such unified atmosphere and wind simulations for O stars. The order of the turbulent velocities is ~ 30 -100 km/s, with higher values for models with higher luminosity-to-mass ratios. This is in general good agreement with observations of photospheric macroturbulence in O stars (Simón-Díaz et al. 2017a), and also overall agree well with results from recent independent three-dimensional (3D) massive-star modelling by Schultz et al. (2023), albeit without

accounting for the effects of line-driving and wind outflows. In that work, the authors used the Monte-Carlo radiative transport framework SEDONA (Kasen et al. 2006) to produce absorption lines from 3D RHD simulations (which were run using ATHENA++, Jiang et al. 2015; Schultz et al. 2022).

In this paper, we present the first results from our 3D unified atmosphere and wind simulations of O stars, focusing here on the spectroscopic signatures of such simulations using 3D radiative transfer techniques to create synthetic images and spectra (building from the general code package presented in Hennicker et al. 2019; Hennicker et al. 2022).

2. 3D unified atmosphere and wind simulations of O-type stars

2.1. RHD simulation method

Previously, Debnath et al. (2024) studied unified atmosphere and wind simulations of O-type stars using the RHD module from Moens et al. (2022b) of MPI-AMRVAC (Xia et al. 2018; Kepens et al. 2023) in 2D. We take their prototypical ‘O4’ model, and use the same numerical setup to here calculate new simulations by solving the time-dependent RHD equations on a finite volume in three spatial dimensions, including correction terms for spherical divergence (see Moens et al. 2022b). This means we solve the equations of mass, momentum, and energy conservation, including the effects of the radiation field in both the total momentum (radiation force) and energy (radiative heating and cooling). Gravity is included for a fixed point stellar mass M_* . The radiation field is computed from the frequency-integrated time-dependent radiation energy equation in the co-moving frame. The necessary closure relations between radiation energy density, pressure, and flux are obtained analytically by a flux-limiting procedure that preserves the optically thick and thin limits. Mean opacities include Rosseland mean opacities and line-driving effects in the same way as first outlined in Poniatowski et al. (2022), and as in previous work we assume the flux, energy, and Planck mean opacities to be the same. For further details, including exact equations as well as specifications of initial and boundary conditions, see Moens et al. (2022a,b); Debnath et al. (2024). The radial direction extends (approximately) thrice the lower boundary radius R_0 . This R_0 is defined as the radius where the temperature in the initial conditions reaches 500 kK, here $\approx 13.54 R_\odot$. Both the tangential directions cover $0.2 R_0$. Radially, the box has 128 grid points for the lowest resolution, and both tangential directions have 16 grid points. The highest level of refinement is level four, which has a resolution that is a factor of 2^3 higher than the lowest resolution (first level).

2.2. Basic characteristics of early O star 3D model

As in the 2D simulations by Debnath et al. (2024), structure starts appearing in our 3D model just below the iron-opacity peak, where the gas and radiation temperature are ~ 200 kK. As energy transport by convection in these atmospheres is inefficient (Debnath et al. 2024), the very sensitive dependence of the Rosseland mean opacity on temperature around the iron opacity peak yields local pockets of gas that are radiatively accelerated exceeding gravity ($g_{\text{rad}} > g_{\text{grav}}$). As a result, these pockets shoot up with velocities higher than the gas sound speed (however less than the gas+radiation sound speed, see Debnath et al. 2024) into the upper and cooler atmosphere. There, Rosseland mean opacities are lower than in the deeper layers, and the gas is decelerated. While some gas parcels fall back into the deep atmosphere,

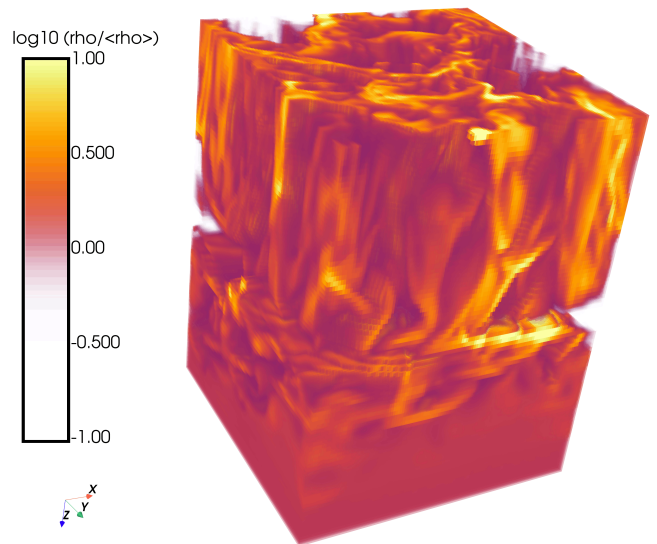


Fig. 1: Volume rendering of relative density (displayed colours are $\log_{10} \rho / \langle \rho \rangle$) for the 3D model atmosphere and wind. Angle brackets denote lateral averaging at each radial position.

others become subject to line-driving and re-accelerate to launch a supersonic wind outflow. This complex interplay creates a very turbulent atmosphere characterised by large density and temperature fluctuations and high velocity dispersions. A more complete analysis of this process has been explored in Debnath et al. (2024) for a set of 2D O star models, and Moens et al. (2022a) for a 3D stripped, hot dwarf model.

Fig. 1 shows a volume rendering of relative density in a selected part of the 3D atmosphere, taken at a snapshot well after the simulation has adjusted from the initial conditions. Relative density here means that the displayed colours are $\log_{10} \rho / \langle \rho \rangle$ where angle brackets denote lateral averaging at each radial position. The 3D rendering shows the part of the atmosphere from just below the ‘iron bump’ where inhomogeneities first occur, across the turbulent and variable photosphere, and into the outflowing line-driven wind (up to 1.5 above the average stellar surface). The figure clearly illustrates the turbulent, filamented, and variable nature of the O star envelope and atmosphere. This can also be seen in Fig. 2, in which we see one snapshot sliced at different laterally averaged electron scattering optical depths (and hence different heights above the inner boundary of the snapshot). The upper three panels correspond to a wind part of the snapshot, the middle three panels are around the optical photosphere and the bottom three deep down in the atmosphere. Inspecting the panels in Fig. 2, it can be seen that these three different regions have different structures, velocities and temperature fluctuations. As noted above, in the deep atmosphere around the iron bump, opacity has a very strong temperature dependence. On the other hand, Rosseland mean opacities are also positively correlated with density, meaning that we sometimes observe blobs of high-density gas around the photosphere that are radiatively accelerated (see also Jiang et al. 2018) and thus have rather high positive velocities (middle panels). By contrast, radiative acceleration due to line-driving is negatively correlated with density implying high density wind regions (upper panels) do not experience efficient line-driving but are rather dragged along (with relatively low velocities) by the surrounding rapidly accelerating low-density wind (see also discussions and figures in Moens et al. 2022a; Debnath et al. 2024). Moreover, radiation

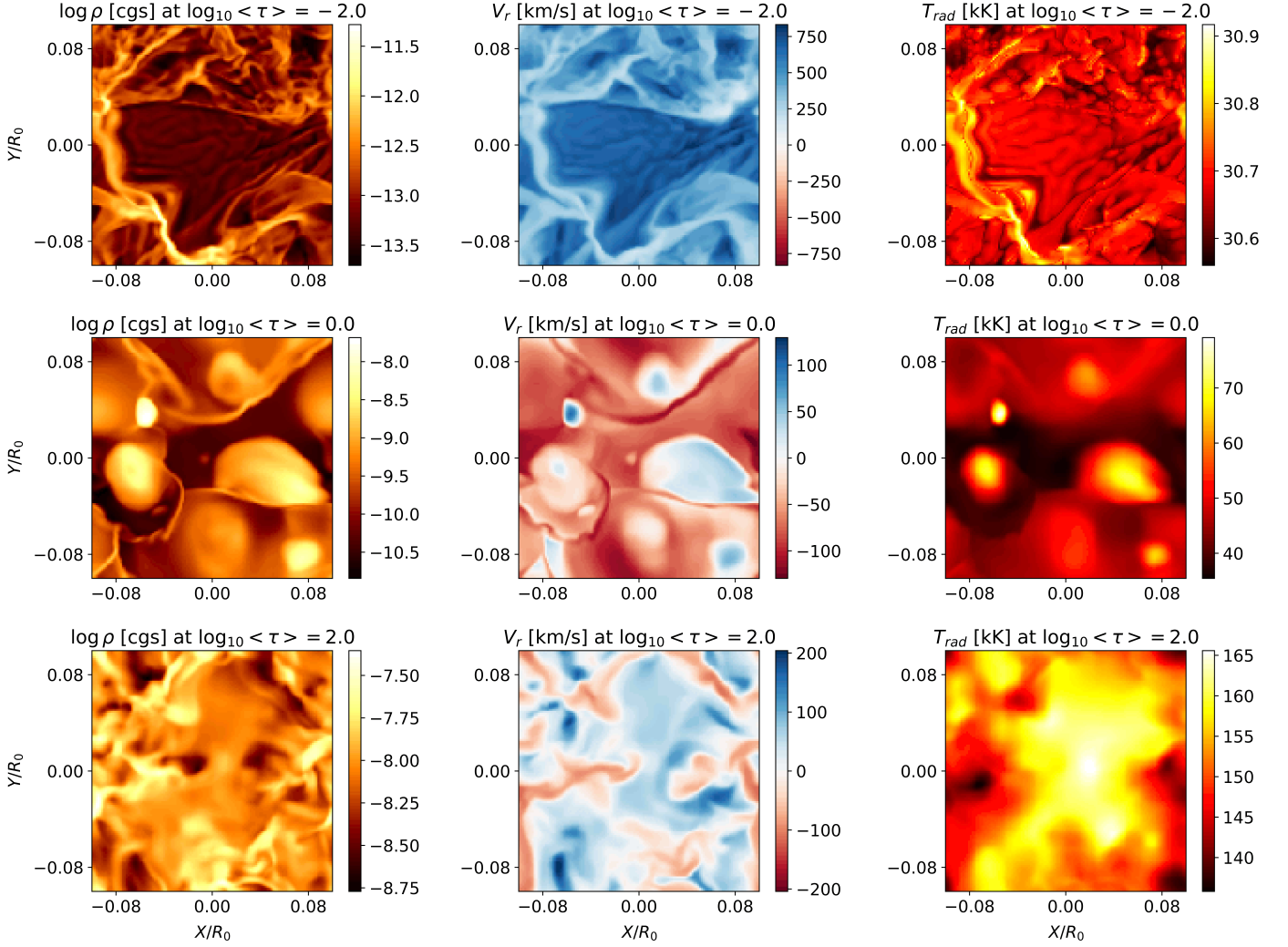


Fig. 2: Maps of logarithm of density, radial velocity, and radiation temperature, in three selected vertical planes with laterally averaged continuum optical depth according to the legends. The lateral X- and Y-axes are labelled in units of R_0 .

temperature fluctuations are highly damped in the wind parts of the simulation as compared to the large fluctuations around the photosphere and in the deeper layers.

Table 1 lists fundamental average parameters of the 3D RHD model. Lateral averages are here taken over 65 snapshots each separated in time by ~ 500 seconds, taken well after the simulation has relaxed from initial conditions. Photospheric parameters are then computed at the average vertical position in the atmosphere corresponding to continuum $\langle \tau_c \rangle = 2/3$, whereas the average mass-loss rate $\langle \dot{M} \rangle$ and maximum wind speed $\langle v_{\max} \rangle$ are taken close to the outer boundary in the outflowing parts of the simulation.¹ Finally the Eddington luminosity is defined as usual, $L_{\text{Edd}} \equiv 4\pi GM_\star c / \kappa_e$, where κ_e is the electron scattering opacity which we also take to be the sole continuum opacity in the computation of the optical depth. Similar to Debnath et al. (2024), we computed that the characteristic dynamical timescale in the deeper atmosphere is on the order of $t_{d,a} \sim 1000$ s, while the dynamical timescale in the wind is on the order of $t_{d,w} \sim 10\,000$ s.

¹ We note that since the average wind is still somewhat accelerating at our outermost grid point (see also Debnath et al. 2024) we need to distinguish between this maximum average wind speed in the simulation and a final terminal wind speed $v_\infty \equiv v_r(r \rightarrow \infty)$.

3. Methodology of radiative transfer calculations

3D radiative transfer techniques (building from Hennicker et al. 2019) are now applied to the 3D unified atmosphere and wind simulations of O stars described above.

3.1. Equations of radiative transfer

Specific intensities are obtained by solving the time-independent equation of radiative transfer:

$$\mathbf{n} \nabla I_\nu = \eta_\nu - \chi_\nu I_\nu = \chi_\nu (S_\nu - I_\nu), \quad (1)$$

where I_ν is the observer's frame specific intensity at frequency ν , η_ν the emissivity, χ_ν the opacity, S_ν the source function and \mathbf{n} the observer's direction. In the main part of this work we assume that opacities and source functions can be calculated locally, using an approximate non-local thermodynamic equilibrium (aNLTE) technique following Lucy & Abbott (1993); Springmann (1997); Puls et al. (2000). This method approximately corrects level population numbers computed in local thermodynamic equilibrium (LTE) by using potentially different radiation and gas temperatures, as well as a modified spherical dilution factor. This modified spherical dilution factor is

Emergent Continuum Intensity

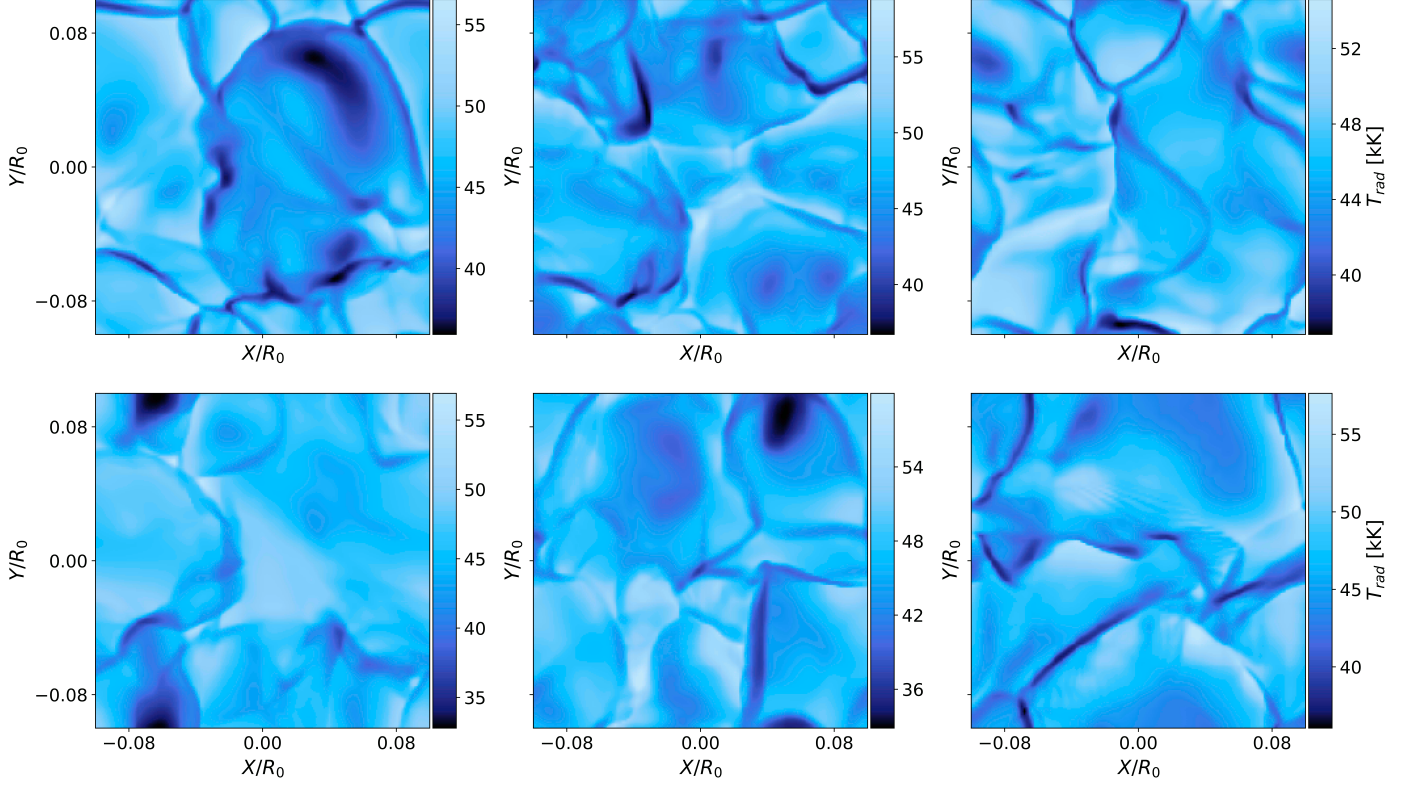


Fig. 3: Emergent optical continuum intensities of local patches on the 3D O star model, for six different snapshots. Colour bars display local emergent radiation temperature defined through $I_\nu \equiv B_\nu(T_{\text{rad}})$. The spatial extent of each X- and Y-axis is $0.2 R_0$.

Table 1: Fundamental parameters for the ⟨3D⟩ O star model studied in this paper. From left to right, the columns display model name, effective temperature, stellar mass, radius, luminosity, Eddington ratio, surface gravity, mass-loss rates, and maximum velocity. Angle brackets denote averaged quantities as explained in the text.

Model	$\langle T_{\text{eff}} \rangle$ [kK]	M_\star/M_\odot	$\langle R_\star \rangle/R_\odot$	$\log_{10} \langle L_\star \rangle / L_\odot$	$\langle L_\star \rangle / L_{\text{edd}}$	$\log_{10} \langle g_\star \rangle$	$\log_{10} \langle \dot{M} \rangle$ [M_\odot/yr]	$\langle v_{\text{max}} \rangle$ [km/s]
O4	40.2	58.3	16.2	5.79	0.27	3.79	-5.90	1800

computed from the mean photospheric radius and optical depth as explained in e.g. [Springmann \(1997\)](#). Local radiation and gas temperatures are here directly taken from the RHD simulation described in the previous section, and the dilution factor is computed from the radially averaged optical depth scale of the model. For continuum opacities and source functions, we assume a constant Thomson scattering opacity and a Planck function using the local gas temperature. In Sect. 6, however, we also provide the first test results from computation of scattering-dominated source functions. In this work, we only treat single lines and we further assume pure Doppler profiles with the widths set by the local thermal speed of the considered ion.

3.2. Emergent intensities and fluxes

The specific intensity found from equation (1) can be used to determine surface intensities of the 3D models. This emergent intensity is then integrated over the projected surface to obtain emergent fluxes. For planar models this is straightforward, but some care must be taken when accounting for sphericity effects. We use a cylindrical coordinate system (for example, [Sundqvist et al. 2012](#), [Hennicker et al. 2022](#)):

$$F_\nu = \frac{1}{d^2} \int_0^{2\pi} \int_0^{R_{\text{max}}} I_{\nu,n}(p, \zeta, z = R_{\text{max}}) p \, dp \, d\zeta, \quad (2)$$

with d being the distance from the observer, R_{max} the maximum size of the emitting object, (p, ζ) the cylindrical coordinates describing the projected disc of the emitting object perpendicular to the observer's direction \mathbf{n} and $I_{\nu,n}(p, \zeta, z = R_{\text{max}})$ the emergent specific intensity into that direction evaluated at a distance $z = R_{\text{max}}$. The z-axis is aligned with the direction to the observer. The geometry is illustrated in Fig. 1 of [Hennicker et al. \(2022\)](#). Radiation is presumed to be free-streaming outside of the simulation domain, as such the intensities at the outer radius do not change until the projected surface at $z = R_{\text{max}}$.

3.3. Building 3D spherical models

Before computing emergent flux line profiles we reconstruct a global 3D spherical model from our local box-in-star RHD simulations. Since the width of the RHD simulations is much smaller than the radius of the star (as can be seen in Figures 2 and 3), we need many (in this specific case 100) simulation boxes (from

here on called snapshots) to cover the full stellar and wind surface. Figure 4a gives a figurative illustration of how typical snapshots look (shape-wise). Once the snapshots are chosen from which the 3D spherical model will be constructed, the selected snapshots are stacked together (see Fig. 4b for an illustration of this process) and transformed into a sphere using cube-sphere transformations. The cubed-sphere coordinates split the sphere into six separate sectors (see Fig. 4c), where each of the sectors has its own local coordinate system (r, ξ, ζ). Here, r is the radial coordinate and ξ and ζ are two angular coordinates. The transformation from our pseudo-planar coordinates from the RHD simulations to the cubed-sphere coordinates, happens by interpreting the radial coordinate from the simulations as the radial coordinate on the cubed sphere, and interpreting the two lateral coordinates as the two angular ones. A final transformation turns this into a spherical star as illustrated in Fig. 4d. See for example Ronchi et al. (1996); Dimitrijevic et al. (2016) for more details on the cube-sphere transformation process.

A justified concern that should be noted is that the cube-sphere transformation (going from Fig. 4b to Fig. 4d) stretches and distorts the atmospheric structures. This distortion grows linearly with the radius as we interpret the lateral coordinate in the RHD simulations as an angular coordinate in the construction of the sphere. Most importantly, however, the radial distance from the stellar core for each point stays the same. Sphericity effects have been accounted for as much as possible already in the RHD simulations (see for example Moens et al. 2022b, Appendix A) and as such the radial structure is consistent.

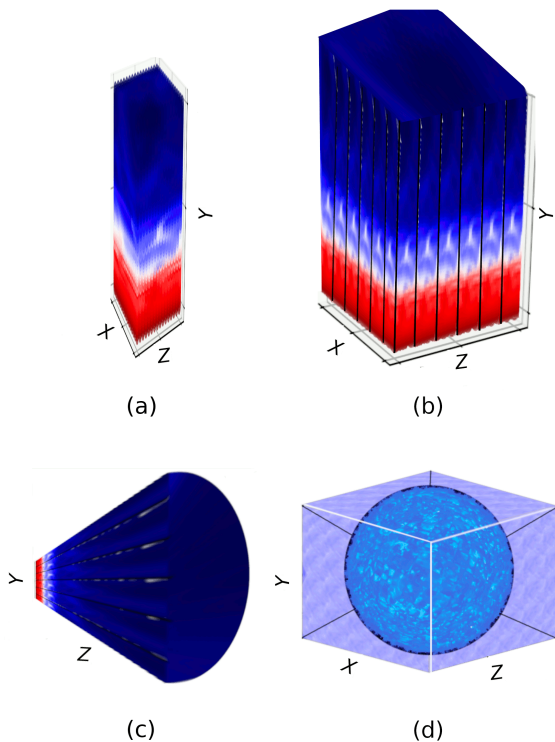


Fig. 4: Figurative illustrations of (a) the snapshots (3D unified atmosphere and wind simulations of O-type stars), (b) the stacked snapshots (stacked-snapshot-array), (c) one of the six sectors that is constructed from our stacked-snapshot-array and (d) the sphere that is constructed. For this illustration only one snapshot was used, hence a repetitive pattern is visible. The colour represents an arbitrary field in the simulation.

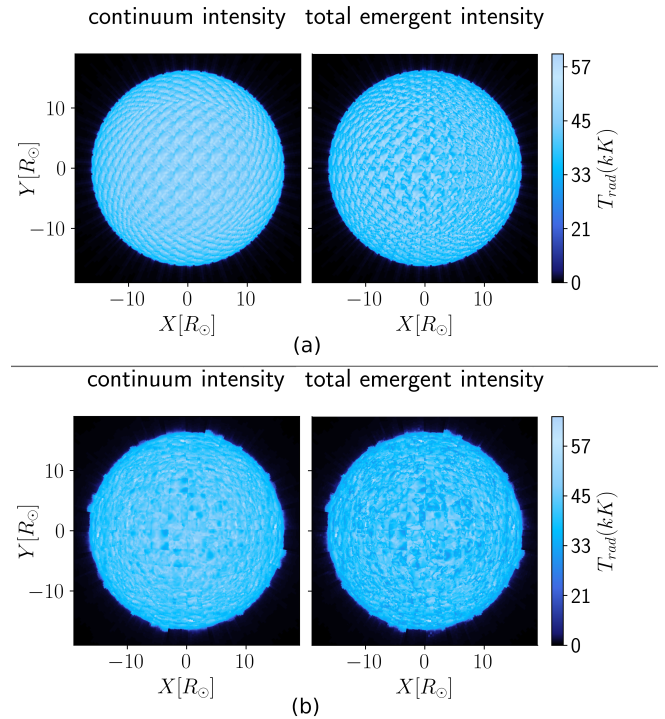


Fig. 5: Surface brightness plots of the O star simulations described above, at the wavelength of the O III 5594 line: (a) for a snapshot-sphere model, (b) for a mixed-sphere model.

In this work, we use a set of 65 snapshots, each spaced approximately $0.5 t_{d,w}$ in time. We build two kinds of 3D spherical models. First, we create ‘snapshot-spheres’. For these models, one snapshot is copied 100 times to construct our stacked-snapshot-array, and in total 600 times to create our full 3D spherical model (since the stacked-snapshot-array is copied six times to form our sphere). Second, we create ‘mixed-spheres’. For these models, we mix our 65 snapshots to build our spherical model. We create 20 mixed-sphere models (in which we make sure that the snapshot placement is different from the other mixed-sphere models). Note that since we need 100 snapshots to assemble our stacked-snapshot-array, we allow that snapshots be used (at most) twice during this construction process. During the spherical model construction and the spectral synthesis process, we degrade the 3D information, and also transform it onto other grids. The final cylindrical grid on which the formal integral is solved, has 397, 157 and 800 points in (p, ζ, z) , respectively. We have tested that doubling this resolution has a negligible impact on the final resulting flux profiles.

4. The resolved O star surface

Before investigating the O star surface of our spherical constructed models we first examine the individual snapshots, which are not subject to the deformations and stretching discussed in section 3.3.

4.1. Continuum variation of local patch on O star surface

Figure 3 displays emergent intensities for six snapshots of our 3D simulation, computed for a typical continuum wavelength in the optical assuming constant electron scattering opacity. The snapshots are separated by ~ 2000 seconds (which is in between



Fig. 6: Surface brightness illustrations for the O III 5594 Å line, the H alpha line, and the C IV 1548 Å line at line center.

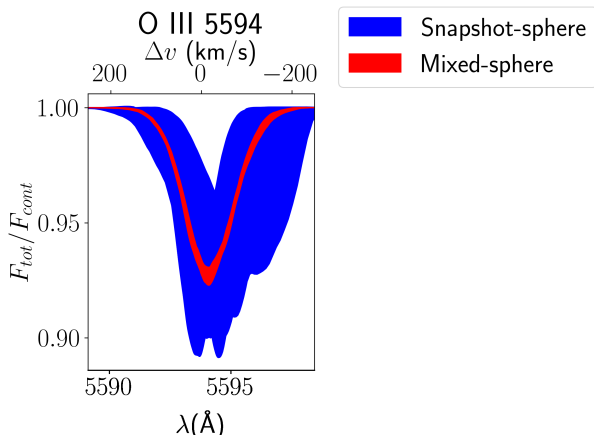


Fig. 7: The coloured-in regions showing variability for the O III 5594 Å line. The blue corresponds to the variability of the snapshot-sphere models (65 models in total), while the red corresponds to the variability of the mixed-sphere models (20 models in total).

the $t_{d,a} \sim 1000$ s and $t_{d,w} \sim 10\,000$ s) and taken well after the model has relaxed and adjusted itself from the initial conditions. The figure shows how the O star surface is characterised by very large spatial and time fluctuations; labelled with the intensities expressed as a radiation temperature $I_\nu \equiv B_\nu(T_{\text{rad}})$, typical surface variations are as high as on order $\sim 10^4$ K. Since the total spatial dimension of these local patches is $0.2 R_0$, the sharp lanes as well as the larger bubble-like features visible in the figure are small in comparison to the star itself. Overall, this reveals a dynamically very active surface in stark contrast with the homogeneous surface assumed by present-day standard 1D models used for spectroscopic studies of O stars.

4.2. Surface brightness maps from spherical models

Using the 3D spherical surface volume reconstruction method described in Sect. 3.3, Figs. 5a and 5b next show two examples of simulated surface brightness plots for the complete star. The first panel in each figure corresponds to the continuum intensity, the second panel to the continuum + line total emergent intensity. We note the visual difference between Figs. 5a and 5b; the former displays a repetitive pattern, as the same snapshot is copied over the entire sphere (the ‘snapshot-sphere’ models). The latter,

on the other hand, fills in the sphere using 65 distinct snapshots and as such avoids the regular patterns. Because of this, we focus primarily on these ‘mixed-sphere’ models in the rest of this work. For example, Fig. 6 displays the emergent intensity at line-centre across the surface for the three key diagnostic lines O III 5594 Å, H α , and C IV 1548 Å. These lines are chosen for Fig. 6 because they represent three different kinds of important diagnostics in O stars (photospheric absorption line, wind-influenced recombination line, UV resonance wind line). As we in practice cannot resolve the O star surface in these wavelengths, the images in Fig. 6 are primarily for illustration purposes. Moreover, since these lines were calculated using an NLTE approach, particularly the C IV 1548 Å line has to be treated with care as this line most definitely has a very scattering-dominated source function (see Sect. 6). Nonetheless, what already can be clearly seen from these images is that this (mixed-sphere) star is very non-uniform, which is in contrast with the typical assumption that massive stars are pretty smooth and stable at the photosphere.

5. Line profile results and trends

5.1. Line profile variability

Spectroscopic line profile variability has been observed in O-type stars (for example Fullerton et al. 1996; Kholtygin et al. 2003; Aerts et al. 2018). In our simulations, variability occurs naturally. Hence, let us first find approximate upper and lower limits of variability predicted by our RHD simulations. This variation in our line profiles can be looked at quite naturally, since it comes directly from our models (something that cannot be done in stationary 1D models). We focus the analysis in this section on three photospheric optical lines of carbon, nitrogen, and oxygen that are often used in spectroscopic analysis of O stars.

A lower limit can be found from the mixed-sphere models (see Sect. 3.3), since these average out the variability of individual snapshots (different assemblies of the same set of snapshots will give similar spectroscopic features). The snapshot-sphere models do not apply such averaging, thus providing approximate upper limits to the variability of emergent flux profiles (different assemblies of different snapshots will give different spectroscopic features).

Fig. 8a displays results from 65 snapshot-sphere models along with the mean flux profile, illustrating a large (and very likely overestimated) level of variability in three characteristic optical absorption lines stemming from this method. Figure 7 compares the typical level of variability from the two spherical

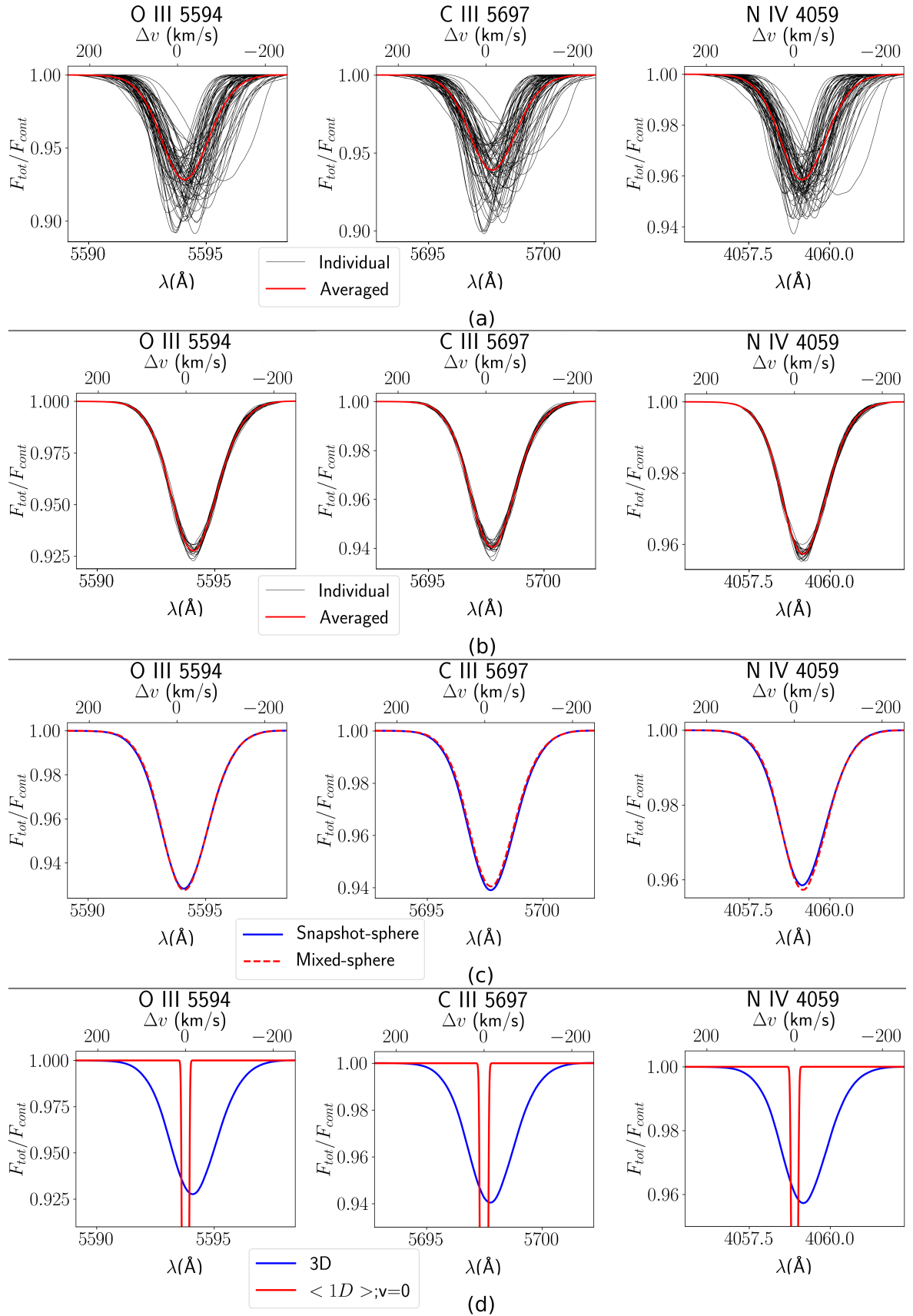


Fig. 8: The O III 5594 Å line, the C III 5697 Å line and the N IV 4059 Å line for the 3D O star simulation, (a) using snapshot-sphere models (the red lines show the result when all lines are averaged), (b) using mixed-sphere models (the red lines show the result when all lines are averaged), (c) showing averaged lines from both the snapshot-spheres (blue line) and mixed spheres (red line) and (d) showing averaged lines for the mixed-sphere models for both the ‘3D’ (unaltered) models and the 1D averaged, velocity-field-turned-off models.

reconstruction methods. As expected, the variability (that can also be seen in Fig. 8b) in the mixed-sphere models is much lower than in the snapshot-sphere models. This can be quantified by calculating the standard deviation of the variability. This standard deviation was calculated for each frequency/wavelength-point of the calculated profile. For clarity, we only provide the standard deviation (in units of normalised flux: $F_{\text{tot}}/F_{\text{cont}}$) at line-centre for each line. For the snapshot-sphere models, they are approximately 0.017 for the O III 5594 Å line, 0.018 for the C III 5697 Å line, and approximately 0.009 for the N IV 4059 Å line. For the mixed-sphere models, these values are approximately 0.0019 for both the O III 5594 Å and the C III 5697 Å line, and 0.0009 for the N IV 4059 Å line. This indeed shows that the variability of the mixed-sphere models is much lower than the variability of the snapshot-sphere models. Importantly, however, the average emergent profiles agree very well between the two methods (as can be seen in Fig. 8c), demonstrating that for the purpose of evaluating gross 3D effects the specific averaging choice is less important.

5.2. Averaged line profiles

We next analyse averaged line profiles, using measurements of average Full Width at Half Maximum (FWHM) and the associated standard deviation σ , as well as the equivalent width (EW). We note that for the calculation of σ , we assume that we are working with an isotropic Gaussian: $\sigma = \text{FWHM}/2 \sqrt{2 \ln(2)}$. The line averaging procedure is a simple averaging, where simulated data at each velocity point are added together and divided by the total number. The results of this averaging for the snapshot-spheres can be found in Fig. 8a, where the red line corresponds to the averaged line, and Fig. 8c, where the blue line corresponds to the averaged line. For the mixed-spheres, the averaged line can be seen in red in Fig. 8b and in red in Fig. 8c. Although there is a clearly visible difference in the variability of these models (as can also be seen in Fig. 7) the averages of the line profiles are almost identical. This shows that even though different model-construction-methodologies were used the average line profiles that emerge are very similar. The resulting FWHM, σ , and EW for the mixed-spheres can be found in Table 2 (see Appendix A for corresponding values for snapshot-spheres, including Tables A1 and A2 for further details).

The results in Table 2 show that for the photospheric lines O III 5594 Å, C III 5697 Å and N IV 4059 Å stemming from our 3D mixed-sphere models, FWHM of the averaged lines lie in between 120 km/s - 130 km/s, with a corresponding σ in the range 52 km/s - 55 km/s. The small differences in FWHMs and σ 's between the lines could be due to them having slightly different formation regions (and hence also slightly different turbulent velocities in the formation regions). Note that these characteristic widths are obtained here directly from the 3D model without any inclusion of ad-hoc micro- or macroturbulence broadening; and indeed, they are on the same order as typical observed photospheric O star line profiles (see the introduction).

5.3. Comparison with 1D, static atmosphere

We next compare the results of our synthetic photospheric line production to corresponding results of 1D codes by re-computing the lines from 1D radial averages of our snapshot-sphere and mixed-sphere models, and setting all velocities to zero. This approach thus mimics what would come out of an equivalent 1D, static model photosphere analysis. For the mixed-

Table 2: FWHMs and EWs of the averaged line profiles of the mixed-spheres shown in Fig. 8d. See Table A1 and A2 for more details.

Model-type	FWHM	σ	EW
(for averaged line)			
O III 5594			
Mixed-sphere	129 km/s	55 km/s	10 km/s
3D	18 km/s	7.5 km/s	3.2 km/s
<1D> ; $v = 0$			
C III 5697			
Mixed-sphere	128 km/s	54 km/s	7.9 km/s
3D	20 km/s	8.3 km/s	3.4 km/s
<1D> ; $v = 0$			
N IV 4059			
Mixed-sphere	123 km/s	52 km/s	5.7 km/s
3D	14 km/s	6.1 km/s	1.9 km/s
<1D> ; $v = 0$			

sphere models, results are shown for the same three lines analysed above in Fig. 8d. The FWHMs, σ 's, and EWs of the mixed-sphere models are given in Table 2. As previously, corresponding values for the snapshot-sphere models can be found in Appendix A. Inspecting Fig. 8d and Table 2 one can see that, as expected, the line profiles for the 1D static model are much narrower (FWHM on the order of 10 km/s - 20 km/s instead of 120 km/s - 130 km/s), and also deeper. This is a direct illustration of the effect the 3D velocity fields have upon photospheric absorption lines, offering a natural explanation for the need of 'extra' ad-hoc broadening mechanisms in 1D model atmosphere codes. Additionally, we note that also the EWs of the lines are different, with the ones computed from 3D models clearly higher (see discussions below). This difference in EWs shows that this broadening is not just a macroscopic broadening effect, but also affects the overall strengths of the lines (most often mimicked in 1D codes by adding ad-hoc 'microturbulence'). Another important note is that the lines in Fig. 8d are slightly shifted toward the red in comparison to the 1D averaged lines. This is due to the fact that the photospheric surface is a dynamic one, and as such, the emitting surface is shifting the line. This net-infall of material around the photosphere was noted also in (Debnath et al. 2024) and can be seen in the middle panel of Fig. 2, which shows that more than half of the surface has infalling material.

6. First line profile results including scattering

This section discusses first test results when line profiles are computed using scattering-dominated source functions. Basic assumptions and methods of this are the following (see Hennicker et al. 2019). The continuum and line source functions S_C and S_L are, respectively:

$$S_C = (1 - \epsilon_C)J_\nu + \epsilon_C B_\nu \quad (3)$$

$$S_L = (1 - \epsilon_L)\bar{J} + \epsilon_L B_{\nu_0}, \quad (4)$$

with ϵ_C and ϵ_L the thermalization parameters (0 is full scattering, 1 is full thermal), J_ν the mean intensity, \bar{J} the profile-weighted mean line intensity and B_{ν_0} the Planck function at line-centre ν_0 . The determination of source functions assumes a two-level atom with a thermal+scattering continuum for the line formation. For these first tests, we simply take both ϵ values as fixed

input parameters (work is underway to instead compute them from atomic line and continuum data). Source functions are derived from 3D short-characteristics (SC) solutions to the equations of radiative transfer, discretised on a non-uniform Cartesian grid. The solution is augmented by an ‘accelerated-lambda-iteration’ (ALI) scheme, using non-local operators to ensure convergence. The procedure is described in detail in Hennicker et al. (2019). The line opacities are still calculated using the approximate NLTE approach described above. The Cartesian grid used for these calculations consists of 219 points along each axis (so 110 in each positive or negative direction of x , y and z).

Including scattering typically reduces source functions in the line forming layers. As a consequence, this could potentially desaturate photospheric lines that may be saturated in our previous results. This is important for future applications, for example comparing synthetic lines to observations, since it can affect the line depths (and hence EWs). We note, however, that in our tests the FWHMs and σ ’s derived above are barely affected by the inclusion of scattering. The deepening effect on the line stemming from scattering can be seen in Fig. 9 for the O III 5594 Å line, which shows that the scattering line source function is significantly depressed as compared to the aNLTE source function.

The scattering line source function also allows us to model the strong UV resonance lines that typically appear as P-Cygni lines in O star spectra. Figure 10 shows the carbon UV resonance line at 1548 Å. In this figure, it is clearly visible that we have a much better P-Cygni wind profile compared to our aNLTE method. Note, however, that the underlying 3D RHD O star simulation does not go out far enough in radius to capture the complete C IV 1548 Å line formation region, which means that we may expect the blue edge of the line to reach somewhat higher velocities than in this figure. Moreover, since the investigated C IV line in reality is a doublet, this must be accounted for before a direct comparison to observations can be done. Nonetheless, the figure illustrates how our 3D models are able to naturally capture key elements of such P-Cygni lines, such as the softening of the blue absorption edge by the turbulent velocity field. In summary, Figs. 9 and 10 show first promising results from using scattering-dominated source functions, taking us one step closer to performing quantitative spectroscopy using 3D models.

7. Discussion and Conclusion

When inspecting our 3D RHD simulation of a typical early O star in the Galaxy, we find turbulent velocities of approximately 48 km/s, alternatively measured as velocity dispersions ($\sigma_{vd}^2 = \langle v_d^2 \rangle = \langle v_r^2 \rangle$) of approximately 57 km/s at the average optical photosphere. Computing averaged photospheric absorption line profiles (see Table 2), we found broadening with standard deviation of approximately 54 km/s. That is, we may directly relate the magnitudes of turbulent velocities measured in the RHD simulations to the typical broadening expected for corresponding absorption line profiles. Moreover, these values are broadly on the same order as typically observed for O stars (for example Simón-Díaz et al. 2010; Simón-Díaz & Herrero 2014; Simón-Díaz et al. 2017a; Serebriakova et al. 2023, 2024).²

This large natural broadening of massive-star absorption lines has been found in other recent 3D modelling as well (Schultz et al. 2023, see for example their Figs. 9 and 10), using

² Note, however, that the so-called ‘macroturbulent velocity’ normally used in spectroscopic studies is not the same quantity as the more general velocity dispersion used here (see Gray 2021 for translations between quantities).

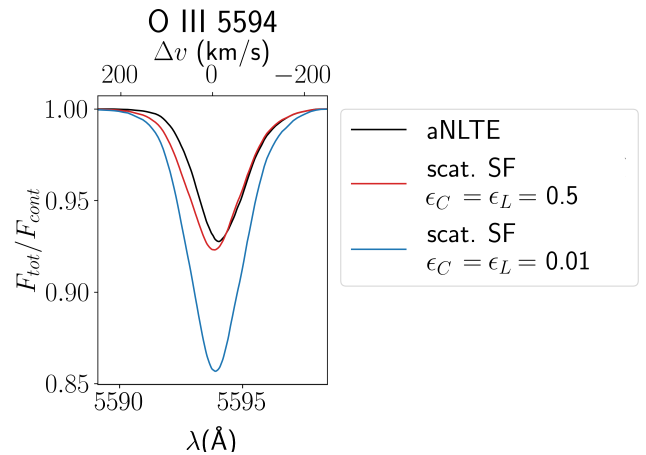


Fig. 9: The O III 5594 Å line for one mixed-sphere model, using two different calculation methods. First, the previously shown aNLTE approach (the black line). Second, the scattering-dominated source function approach (red and blue line). Note that the difference between the red and blue line is the used values of the thermalization parameters ϵ_C and ϵ_L .

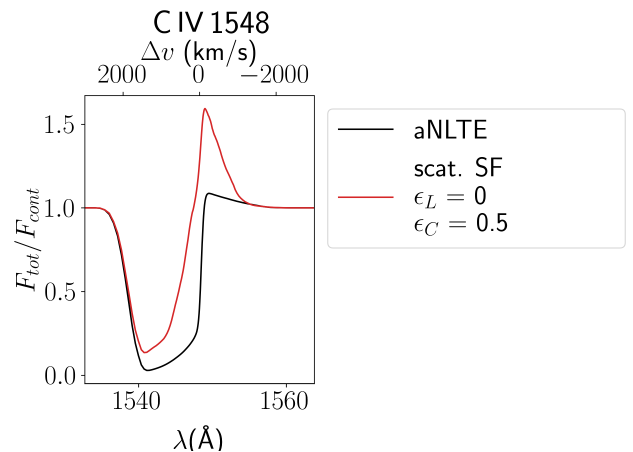


Fig. 10: The C IV 1548 Å line for one mixed-sphere model, using two different calculation methods. First, the previously shown aNLTE approach (the black line). Second, the scattering-dominated source function approach (red line).

Monte-Carlo radiative transport to produce absorption lines from the 3D ATHENA++ RHD simulations by Jiang et al. (2015); Schultz et al. (2022). Since their chosen massive stars to model do not have the same fundamental parameters as the O star presented here, the broadening results can however not be directly quantitatively compared. Also, in addition to different radiative transfer techniques, the underlying 3D RHD simulation methods differ between the two groups, as their ATHENA++ framework on the one hand uses a more sophisticated radiation closure (based on an Eddington tensor method), but on the other hand does not account for line-driving effects (thus their simulations lack a wind outflow). Nonetheless, the overall qualitative agreement in results stemming from these two independent developments is very reassuring for future 3D massive-star model atmosphere work.

In addition to line-broadening, the average atmospheric properties also change in multi-D simulations. Perhaps most strikingly for O stars, the strong turbulent pressure results in

much larger photospheric scale-heights, and thus in significantly shallower density profiles (see also [Debnath et al. 2024](#)). As recently investigated by [González-Torà et al. \(2025\)](#) this affects in particular surface gravity determinations from observed spectral line profiles, and it is suggested that this might present a solution to the so-called ‘mass-discrepancy problem’ that is seen between evolutionary and spectroscopy mass determinations ([Herrero et al. 1992](#)). In this paper we have demonstrated how the photospheric turbulent velocity is directly related to the measured dispersion of absorption lines. While awaiting full 3D-based spectroscopic studies, one may thus use observed velocity dispersions in photospheric lines (at least in the absence of dominant rotational broadening) to calibrate the turbulent velocity needed to correct the hydrostatic equations used in all present-day 1D atmospheric models.

Finally, we note that we have potential 3D-effects on abundance determinations, since the EWs found for the lines are different than in corresponding 1D models. This may lead to differences in derived abundances for the same objects, although the relative role of such 3D abundance corrections and the ‘microturbulence’ used in 1D models is not clear at the present (also since this strongly depends on the treatment of line scattering which will be further studied in future work). Comparing to studies on low-mass stars, abundance determinations done using 3D (time-dependent hydrodynamical) models of the Sun’s atmosphere have even changed the solar chemical composition yardstick ([Asplund et al. 2009](#)). For such low-mass stars in general, studies over the past decade have shown that results derived from 1D average structures are not adequate as substitutes for full 3D spectroscopy ([Lind & Amarsi 2024](#)).

In this paper we have shown first promising results toward spectroscopy using 3D models also for hot, massive stars. In future work, we will extend our formalism to include doublets, damping wings, as well as full scattering and NLTE effects, thus enabling direct comparison to observations by means of quantitative spectroscopy.

Acknowledgements. The computational resources used for this work were provided by Vlaams Supercomputer Centrum (VSC) funded by the Research Foundation-Flanders (FWO) and the Flemish Government. The authors gratefully acknowledge support from the European Research Council (ERC) Horizon Europe under grant agreement number 101044048, from the Belgian Research Foundation Flanders (FWO) Odysseus program under grant number G0H9218N, from FWO grant G077822N, and from KU Leuven C1 grant BRAVE C16/23/009. The authors would also like to thank previous members of the KUL-EQUATION group for their earlier contributions. Finally, the authors would like to thank all members of the KUL-EQUATION group for fruitful discussion, comments, and suggestions. LD would also like to thank Conny Aerts for giving feedback on the draft, Levin Hennicker for the help and discussions in order to understand the general code package better and Stan Owoc for the discussions and insights. We made significant use of the following packages to analyse our data: NumPy ([Harris et al. 2020](#)), SciPy ([Virtanen et al. 2020](#)), matplotlib ([Hunter 2007](#)), Python amrvac_reader ([Keppens et al. 2020](#)), PyVista ([Sullivan & Kaszynski 2019](#)).

References

- Aerts, C., Bowman, D. M., Símón-Díaz, S., et al. 2018, *MNRAS*, 476, 1234
 Asplund, M., Grevesse, N., Sauval, A. J., & Scott, P. 2009, *ARA&A*, 47, 481–522
 Blaes, O. & Socrates, A. 2003, *ApJ*, 596, 509
 Cantiello, M., Langer, N., Brott, I., et al. 2009, *A&A*, 499, 279
 Castor, J. I., Abbott, D. C., & Klein, R. I. 1975, *ApJ*, 195, 157
 Conti, P. S. & Ebbets, D. 1977, *ApJ*, 213, 438
 Debnath, D., Sundqvist, J. O., Moens, N., et al. 2024, *A&A*, 684, A177
 Dimitrijevic, A. M., Lambers, M., & Rancic, D. D. 2016, in *COMPARISON OF SPHERICAL CUBE MAP PROJECTIONS USED IN PLANET-SIZED TERRAIN RENDERING*
 Eversberg, T., Lépine, S., & Moffat, A. F. J. 1998, *ApJ*, 494, 799
 Fullerton, A. W., Gies, D. R., & Bolton, C. T. 1996, *ApJS*, 103, 475
 González-Torà, G., Sander, A. A. C., Sundqvist, J. O., et al. 2025, *A&A*, 694, A269
 Gray, D. F. 2021, *The Observation and Analysis of Stellar Photospheres*, 4th edn. (Cambridge University Press)
 Harris, C. R., Millman, K. J., van der Walt, S. J., et al. 2020, *Nature*, 585, 357
 Hearn, A. G. 1972, *Astron. Astrophys.* 19: No. 3, 417–26 (Jul 1972).
 Hennicker, L., Kee, N. D., Shenar, T., et al. 2022, *A&A*, 660, A17
 Hennicker, L., Puls, J., Kee, N., & Sundqvist, J. 2019, *A&A*, 633
 Herrero, A., Kudritzki, R. P., Vilchez, J. M., et al. 1992, *A&A*, 261, 209
 Hillier, D. J. & Miller, D. L. 1998, *ApJ*, 496, 407
 Hunter, J. D. 2007, *Computing in Science and Engineering*, 9, 90
 Iglesias, C. A. & Rogers, F. J. 1996, *ApJ*, 464, 943
 Jiang, Y.-F., Cantiello, M., Bildsten, L., Quataert, E., & Blaes, O. 2015, *ApJ*, 813, 74
 Jiang, Y.-F., Cantiello, M., Bildsten, L., et al. 2018, *Nature*, 561, 498
 Kasen, D., Thomas, R. C., & Nugent, P. 2006, *ApJ*, 651, 366
 Keppens, R., Popescu Braileanu, B., Zhou, Y., et al. 2023, *A&A*, 673, A66
 Keppens, R., Teunissen, J., Xia, C., & Porth, O. 2020, *arXiv e-prints*, arXiv:2004.03275
 Key, J. A., Proga, D., Dannen, R., Vivier, S., & Waters, T. 2025, *ApJ*, 987, 144
 Kholtygin, A. F., Monin, D. N., Surkov, A. E., & Fabrika, S. N. 2003, *Astronomy Letters*, 29, 175
 Kudritzki, R.-P. & Puls, J. 2000, *ARA&A*, 38, 613
 Lind, K. & Amarsi, A. M. 2024, 3D non-LTE abundance analyses of late-type stars
 Lucy, L. B. & Abbott, D. C. 1993, *ApJ*, 405, 738
 Moens, N., Poniatowski, L. G., Hennicker, L., et al. 2022a, *A&A*, 665, A42
 Moens, N., Sundqvist, J. O., El Mellah, I., et al. 2022b, *A&A*, 657, A81
 Owoc, S. P. & Rybicki, G. B. 1984, *ApJ*, 284, 337
 Poniatowski, L. G., Kee, N. D., Sundqvist, J. O., et al. 2022, *A&A*, 667, A113
 Poniatowski, L. G., Sundqvist, J. O., Kee, N. D., et al. 2021, *A&A*, 647, A151
 Puls, J., Markova, N., Scuderi, S., et al. 2006, *A&A*, 454, 625
 Puls, J., Springmann, U., & Lennon, M. 2000, *A&AS*, 141, 23
 Puls, J., Urbaneja, M. A., Venero, R., et al. 2005, *A&A*, 435, 669–698
 Ronchi, C., Iacono, R., & Paolucci, P. 1996, *Journal of Computational Physics*, 124, 93
 Sander, A., Hamann, W.-R., & Todt, H. 2012, *A&A*, 540, A144
 Schultz, W. C., Bildsten, L., & Jiang, Y.-F. 2022, *The Astrophysical Journal Letters*, 924, L11
 Schultz, W. C., Tsang, B. T.-H., Bildsten, L., & Jiang, Y.-F. 2023, *ApJ*, 945, 58
 Serebriakova, N., Tkachenko, A., & Aerts, C. 2024, *A&A*, 692, A245
 Serebriakova, N., Tkachenko, A., Gebruers, S., et al. 2023, *A&A*, 676, A85
 Símón-Díaz, S., Godart, M., Castro, N., et al. 2017a, *A&A*, 597, A22
 Símón-Díaz, S., Godart, M., Castro, N., et al. 2017b, *A&A*, 597, A22
 Símón-Díaz, S. & Herrero, A. 2014, *A&A*, 562, A135
 Símón-Díaz, S., Herrero, A., Uytterhoeven, K., et al. 2010, *ApJ*, 720, L174–L178
 Sobolev, V. V. 1960, *Moving Envelopes of Stars*
 Springmann, U. 1997, *On the theory of radiation driven winds of Wolf-Rayet stars*
 Sullivan, B. & Kaszynski, A. 2019, *Journal of Open Source Software*, 4, 1450
 Sundqvist, J. O., Puls, J., & Feldmeier, A. 2010, *A&A*, 510, A11
 Sundqvist, J. O., ud-Doula, A., Owoc, S. P., et al. 2012, *MNRAS*, 420
 Van der Sijpt, C., Sundqvist, J. O., Debnath, D., Driessen, F. A., & Moens, N. 2025, *A&A*, 694, A54
 Virtanen, P., Gommers, R., Oliphant, T. E., et al. 2020, *Nature Methods*, 17, 261
 Xia, C., Teunissen, J., Mellah, I. E., Chané, E., & Keppens, R. 2018, *ApJS*, 234, 30

Appendix A: tables

Table A1: Summary of EWs of the line profiles computed in this work.

Model-type	Average EW (individual lines)	[Min; Max] EW (individual lines)	EW (averaged line)
O III 5594			
Snapshot-sphere			
3D	10.03 km/s	[7.15; 12.49] km/s (range = 5.34 km/s)	9.97 km/s
<1D> ; v = 0	3.48 km/s	[2.45; 4.34] km/s (range = 1.89 km/s)	3.48 km/s
Mixed-sphere			
3D	9.91 km/s	[9.53; 10.09] km/s (range = 0.56 km/s)	9.9 km/s
<1D> ; v = 0	3.19 km/s	[3.04; 3.3] km/s (range = 0.26 km/s)	3.19 km/s
C III 5697			
Snapshot-sphere			
3D	8.27 km/s	[4.52; 10.83] km/s (range = 6.31 km/s)	8.23 km/s
<1D> ; v = 0	3.79 km/s	[2.63; 4.85] km/s (range = 2.22 km/s)	3.79 km/s
Mixed-sphere			
3D	7.9 km/s	[7.5; 8.19] km/s (range = 0.69 km/s)	7.89 km/s
<1D> ; v = 0	3.42 km/s	[3.26; 3.56] km/s (range = 0.3 km/s)	3.42 km/s
N IV 4059			
Snapshot-sphere			
3D	5.66 km/s	[4.38; 7.6] km/s (range = 3.22 km/s)	5.62 km/s
<1D> ; v = 0	2.06 km/s	[1.11; 2.77] km/s (range = 1.66 km/s)	2.06 km/s
Mixed-sphere			
3D	5.69 km/s	[5.59; 5.77] km/s (range = 0.18 km/s)	5.69 km/s
<1D> ; v = 0	1.86 km/s	[1.8; 1.93] km/s (range = 0.13 km/s)	1.86 km/s

Table A2: Summary of FWHMs of the line profiles computed in this work.

Model-type	Average FWHM (individual lines)	[Min; Max] FWHM (individual lines)	Average σ (individual lines)	FWHM (averaged line)	σ (averaged line)
O III 5594					
Snapshot-sphere					
3D	123.88 km/s	[81.71; 182.84] km/s (range = 101.12 km/s)	52.61 km/s	132.72 km/s	56.36 km/s
<1D> ; $v = 0$	17.64 km/s	[15.87; 18.53] km/s (range = 2.66 km/s)	7.49 km/s	17.6 km/s	7.47 km/s
Mixed-sphere					
3D	128.41 km/s	[118.8; 138.31] km/s (range = 19.51 km/s)	54.53 km/s	129.26 km/s	54.89 km/s
<1D> ; $v = 0$	17.6 km/s	[17.6; 17.6] km/s (range = 0.0 km/s)	7.47 km/s	17.6 km/s	7.47 km/s
C III 5697					
Snapshot-sphere					
3D	122.12 km/s	[82.42; 183.06] km/s (range = 100.64 km/s)	51.86 km/s	130.99 km/s	55.63 km/s
<1D> ; $v = 0$	19.5 km/s	[16.71; 21.6] km/s (range = 4.89 km/s)	8.28 km/s	19.5 km/s	8.28 km/s
Mixed-sphere					
3D	126.3 km/s	[115.11; 136.66] km/s (range = 21.55 km/s)	53.63 km/s	127.57 km/s	54.17 km/s
<1D> ; $v = 0$	19.5 km/s	[19.5; 19.5] km/s (range = 0.0 km/s)	8.28 km/s	19.5 km/s	8.28 km/s
N IV 4059					
Snapshot-sphere					
3D	118.7 km/s	[71.17; 178.9] km/s (range = 107.73 km/s)	50.41 km/s	128.18 km/s	54.43 km/s
<1D> ; $v = 0$	14.75 km/s	[13.57; 15.87] km/s (range = 2.3 km/s)	6.26 km/s	15.07 km/s	6.4 km/s
Mixed-sphere					
3D	125.47 km/s	[120.66; 137.92] km/s (range = 21.55 km/s)	53.28 km/s	122.77 km/s	52.14 km/s
<1D> ; $v = 0$	14.3 km/s	[14.3; 14.3] km/s (range = 0.0 km/s)	6.07 km/s	14.3 km/s	6.07 km/s